




Blast Wave Interaction with Generic Objects and the Measurement of Blast Wave Reattachment Distances

Santanu Dey^{1,2} · Thangadurai Murugan^{1,2} · Dipankar Chatterjee^{1,2} 

Received: 24 January 2018 / Accepted: 15 June 2020 / Published online: 26 June 2020
© The Institution of Engineers (India) 2020

Abstract The interaction of blast waves with inanimate and biological structures has remained a subject of interest in order to understand their responses to the blast exposure. In this article, the interaction of blast wave with three generic objects namely sphere, cylinder and cone is studied through numerical simulation. The blast wave is generated in a shock tube by limiting its driver section length. The numerical simulation is carried out by solving the Euler equations using ANSYS-Fluent CFD software. The main focus here is to find the typical object shape for which the blast wave gets regenerated earlier at the rear of the object after reflection and diffraction. It is observed that the reattachment occurs first in case of a sphere, followed by the cone and finally the cylinder.

Keywords Blast wave reattachment · CFD · Blast wave interaction · Shock tube · Vortex ring

Introduction

The blast wave generated from high explosives is extremely harmful especially when one is very close to the explosive core or at a location of the constructive interference. It wraps around any objects and buildings [1] like an acoustic wave. Therefore, persons or objects stay behind the objects are not necessarily protected from a blast which

happens on the opposite side of the building. The intensity of the blast is characterized by the peak overpressure and the impulse, i.e., positive overpressure multiplied by its duration. The intensity/strength of the blast wave behind the objects depends on the nature of the objects, such as regular or irregular, surface topology, number of reflective and diffractive surfaces, etc. The blast wave after wrapping around the object propagates radially outwards, and its strength and speed are initially less compared to the blast wave expanding in the free field along other directions. However, this blast wave gets regenerated at a downstream location after passing over the objects.

The measured blast wave reattachment distances will show the level of blast wave being mitigated/attenuated through the structures without examining the blast wave diffraction, and reflection taking place over the objects in detail. It helps in design and optimization of blast wave mitigating/attenuating devices. Scientists use sophisticated mathematical models for predicting the response of the objects subjected to a blast wave in designing the efficient barriers and safer buildings [2]. Accordingly, the understanding of blast wave interaction with inanimate and biological objects is extremely important in avoiding or reducing the excessive damage caused by the blast wave.

The strength of the blast waves at a given location during field tests is measured using the piezoelectric sensors. These sensors are very costly as they are incorporated with integral electronics and acceleration-compensating sensing elements. When a blast wave is generated through explosives, there is possibility of fragments and debris [3] coming out from the explosion which may hit and damage the costly sensors. Hence, some generic objects are often kept in front of the sensors at some distance during explosive trials to avoid the collision with fragments and debris. Positioning the sensors very close to the objects

✉ Dipankar Chatterjee
d_chatterjee@cmeri.res.in

¹ CSIR-Central Mechanical Engineering Research Institute, Durgapur 713209, India

² Academy of Scientific and Innovative Research, Ghaziabad 201002, India

may yield improper strength of the blast wave. The sensors placed at or after the location of blast wave regeneration yield the peak overpressure and impulse with an acceptable variation ($\leq 5\%$). The blast wave has a characteristic to regenerate after passing over different objects due to their spherical nature. The reattachment distance depends on the blast wave strength and the size and shape of the objects. The exact location of blast wave reattachment from different objects is essential for obtaining the accurate blast wave strength at a given location which is the main focus of the present study.

When a blast wave passes over an elastic object, a part of it gets reflected and moves opposite to the direction of the incident blast wave. A portion is refracted through the object, and some part is diffracted over the object. The blast wave gets reflected upon reaching the rear end and finally attaches with the incident blast wave [4]. Bryson et al. [5] performed experimental studies on diffraction of shock wave around a cylinder, sphere, and cone for shock Mach numbers (M) of 2.85 and 4.41. They compared their results with the theory proposed by Whitham [6, 7] and observed very good agreement with the theory. Sun et al. [8] carried out a numerical study to examine drag experienced by the sphere as shock wave passed over it for $M = 1.22$ and validated their numerical results with the experiments. They found that the numerical simulation through Euler equations could be used for calculating the unsteady drag coefficient acting on the sphere until the shock wave passes over the sphere. They concluded that the viscous drag is negligible when the shock passes over the sphere. However, it became significant after the shock moves away from the sphere due to vorticity production at the shear layer.

Many studies are existing in the literature on shock wave interactions with objects. However, limited studies are available on the interaction of blast wave with objects [9–11] where the primary focus was on understanding the shock cell structures, characterizing the impinging jet and compressible vortex ring. Murugan et al. [12] examined numerically the interaction of blast wave with solid obstacles to find the blast load acting on these objects for incident shock Mach numbers of 2.1 and 3.1. They used helium with a pressure ratio of 13 and 56 in driver section for generating a high peak overpressure blast wave. They have noticed that the load acting on the cuboid (circular disc) was very high compared to the sphere and wedge having the same hydraulic diameter. A similar numerical study was also performed by Dey et al. [13] using air as driver section gas. They found that the blast load acting on the circular disc was 2.09 times more compared to the load acting on a conical object having the same hydraulic diameter for $M = 1.15$. In the present article, the instantaneous pressure field around the three objects namely

sphere, cone, and cylinder during the blast wave interaction and the minimum blast wave regeneration distance behind these objects after the interaction for $M = 1.15$ are obtained which are not available in the existing literature of blast wave. Here, a shock tube having a short driver section length is used for simulating the blast wave [14, 15] as a larger driver section produces stronger jet at the shock tube exit which minimizes the distance between the blast wave and the starting compressible vortex ring [16].

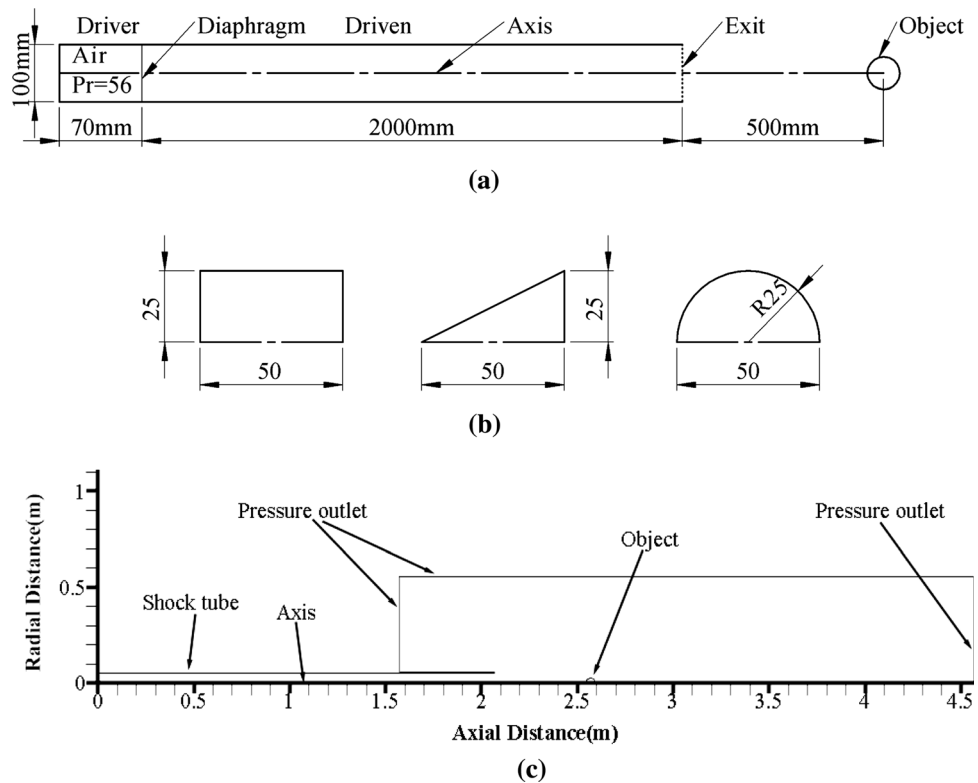
Geometry and Numerical Procedure

Figure 1a shows the dimensions of the shock tube used in the simulation for generating the blast wave. Here, only one-half of the shock tube and objects are simulated as the flow is considered to be symmetric with respect to the shock tube axis [15]. The driver and driven section lengths of the shock tube are 70 mm and 2000 mm, respectively. The objects are placed at 500 mm from the shock tube exit. Figure 1b shows the dimensions of the cylinder, sphere, and cone used in the simulation. The frontal area/height of all the objects is kept same for comparing the strength of blast wave reflection, diffraction, and reattachment distance.

Figure 1c shows the computational domain which includes the driver and driven section of the shock tube, object and the ambient space where the blast wave expands spherically [13]. The model and the meshing are done using GAMBIT software. There are 500 cells placed uniformly in the axial direction (L) inside the driver section (70 mm). The driven section is discretized with 2000 cells in the axial direction where a finer mesh is used close to the shock tube exit, and it is stretched towards the inside portion of the driven section. Two hundred cells are placed uniformly in the lateral (y) direction which is much higher than the number of cells considered in the earlier studies [14, 17, 18] to resolve the shear layer vortices originating at the trailing jet [17].

The objects are kept at distances five times the diameter of the shock tube (D) from the shock tube exit. A very fine mesh is used close to the objects to resolve the development of slipstream shear layers. The first cell size for the cylinder, cone and sphere is 0.25 mm, 0.114 mm and 0.05 mm, respectively. The grid is stretched away from the object in the downstream direction. The pressure outlet boundary is kept at 2 m from the object in the downstream direction to avoid interaction of any wave reflection from the open boundary. A total of 2,358,200 quadrilateral cells are used for discretizing the domain containing the cylinder. A total of 1,931,012 and 2,506,463 cells are used for domains having sphere and cone [13]. No-slip boundary condition is used at the shock tube walls and the surface of

Fig. 1 **a** Schematic of the shock tube with dimensions, **b** schematic of the objects with dimensions and **c** computational domain with object and boundary conditions



the objects. Pressure outlet with non-reflecting acoustic wave model is used at the open boundaries along the axial and lateral directions.

Numerical simulations are performed using ANSYS-Fluent software [19]. The density-based solver is chosen as the flow is compressible and the transient flow is solved with the explicit formulation. Euler equations (inviscid flow) are solved in the axisymmetric form along with energy and state equations as it was shown in many articles that the viscosity has the negligible role on the evolution and interaction of blast wave with objects [18, 20, 21]. The convective terms are calculated using the AUSM scheme [22] coupled with a second-order upwind scheme. It belongs to the flux-vector splitting family of schemes and is known for its low numerical dissipation which is essential for solving the shock dominated flows. This scheme is selected due to the authors experience in solving the compressible shock dominated impinging jet [10, 11]. The solution is initialized with ambient pressure and temperature of 101,325 N/m² and 303 K everywhere. This temperature is chosen based on the average temperature in our laboratory. Then, the driver section is patched with the pressure of 56 times the ambient pressure before calculating the solution. Air is considered as the working fluid. The Courant number is assumed as 0.5, and the convergence criterion of residuals is kept at 10⁻⁵ for flow variables, continuity, and energy equations. The convergence took

place much earlier than the maximum interactions of 500,000 kept for $\mu\mu$ each time step.

Experimental Validation

A quantitative comparison of the speed of the blast wave inside the shock tube and a qualitative comparison of the impulsive jet formed at the exit of the shock tube are used for validating the numerical simulation due to the non-availability of the high frequency static pressure sensors and optical systems (Schlieren, shadowgraph, etc.) in the laboratory. The experimental setup is similar to the one given in Ref. [16]. Figure 2a shows the pressure signals obtained inside the shock tube at two different locations for calculating the speed and incident Mach number of the blast wave. Here, the driver section length is chosen as 112 mm for validating the numerical results though all simulations are performed with 70 mm driver section length. The minimum possible driver section length in our shock tube facility is 112 mm as sufficient space is needed for proving the compressed gas into the driver section length and installing the pressure relief valve for safety. The experiments are performed with a driver section pressure and temperature of 854,950 Pa and 293.15 K. The pressure and temperature inside the laboratory are 101,026 Pa, and 293.15 K which are measured using SATO barometer and digital thermometer. Air is used in

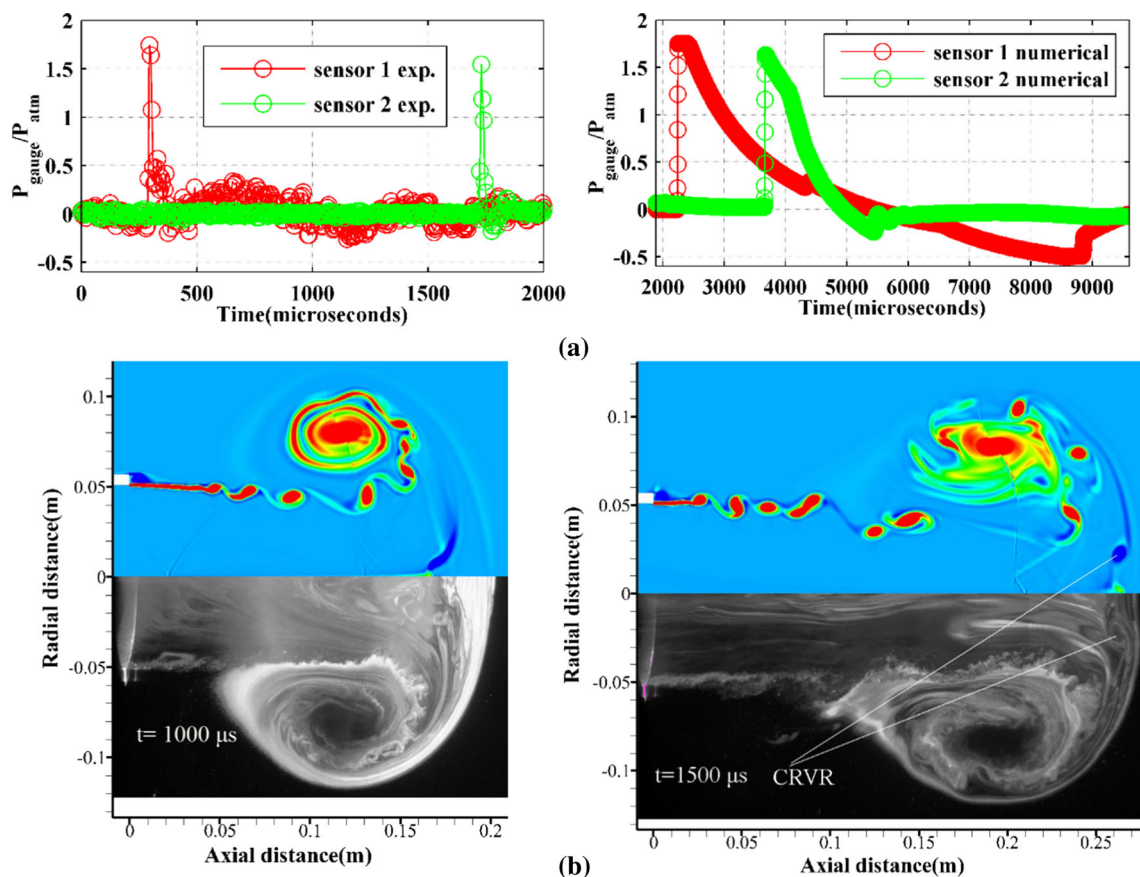


Fig. 2 **a** Comparison of pressure histories from experiment and numerical simulation and **b** comparison of starting jet from numerical simulation with smoke flow visualizations

the driver section. Mylar sheet having a thickness of 250 microns is used as a diaphragm.

The left frame in Fig. 2a shows the pressure histories obtained using two PCB pressure transducers (Model no:132A35) flush mounted inside the shock tube at 50 mm, and 800 mm from the shock tube exit. Model 132A35 is a time of arrival sensor which has a sensitivity of 140 mv/psi. It has a rise time of less than $3 \mu\text{s}$ which helps in accurate prediction of shock speed. It also has an internal 8 kHz high-pass filter for eliminating low-frequency components in the signal. The pressure data were acquired at a frequency of 200 kHz through NI PXI 4462, 24-bit DAQ card using LABVIEW program. The voltage signal is converted into pressure signal using the sensitivity of the sensors. Only a portion of the signal where the blast signature presents is shown in the figure as the data were acquired continuously. The right frame in Fig. 2a shows the pressure histories obtained from the numerical simulation where reference time $t = 0$ is the starting time of the simulation. The initial conditions in the simulation are same as the experiments.

The shock speed is calculated from the time of arrival of shock at the given sensor locations and the known distance from the sensors. The measured shock speed is 522.6 m/s in 7 out of 10 experiments. It was varying from 515 to 531 m/s. The maximum uncertainty in experiments is $\pm 1.5\%$, and it is due to irregular rupture of the Mylar diaphragm [16]. The shock speed measured from the numerical simulation is 528.5 m/s. The variation in shock speed from numerical simulations and experiments is around 1%.

Figure 2b shows the comparison of vorticity field obtained from numerical simulation with the qualitative smoke flow visualizations obtained at the shock tube exit at times $1000 \mu\text{s}$ and $1500 \mu\text{s}$, respectively. The vorticity field is obtained from Tecplot by importing the data from Fluent. Here time $t = 0$ is the position of the blast wave at the tube exit. First, smoke flow visualizations are performed by placing the camera and laser at different locations downstream of the shock tube exit. The vorticity field corresponding to the experiment is obtained by matching the diameter of the shock tube and the position of the vortex ring core from the shock tube exit. Simulations are

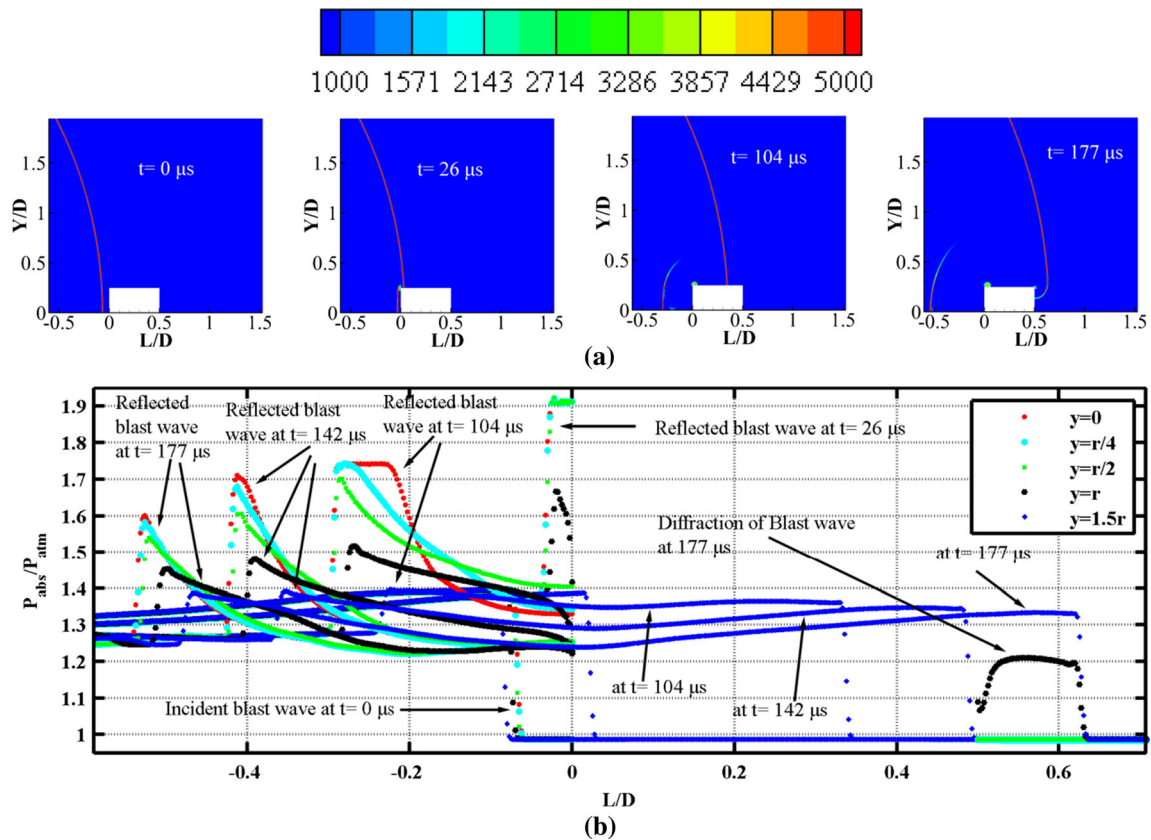


Fig. 3 **a** Density gradient magnitude plots and **b** static pressure variation showing blast wave interaction with cylindrical object for time varying from 0 to 177 μs

performed with every 1 μs to match the experimental results. Flow visualizations are performed by illuminating the smoke particles using a laser sheet from the EverGreen laser (532 nm, 200 mJ/pulse, and 15 Hz double pulsed Nd:YAG laser) from Quantel, France. The shock tube driven section is seeded with an optimum amount of 10 μ size smoke particles before rupturing the diaphragm. A 4 MP CCD camera is used for capturing the flow field [16], and the timing of laser and camera is controlled using a 250 picosecond timer box from TSI India [23] which receives the trigger signal from the pressure transducer.

The flow visualization at $t = 1000 \mu s$ shows the penetration of trailing jet vortices into the vortex ring and a similar trend is observed in simulation. The trailing jet vortices are also resolved well compared to the earlier studies [15, 18] due to higher spatial resolution though it also depends on the selection of solver [24]. At $t = 1500 \mu s$, the counter-rotating vortex ring (CRVR) formed ahead of the vortex ring [16] is predicted well in simulation and the size of the CRVR is also matching quite well. As many studies on the mechanism of CRVR formation and their evolution existed in the literature [16, 18], it is not discussed in the paper. Further, the formation of

CRVR in both experiments and numerical simulation ensures an accurate prediction of flow in simulation as the formation of CRVR is highly sensitive to the flow condition at the exit [25]. This suggests that the inviscid flow simulation is a good choice for examining the blast wave interaction with objects. Further, a grid independence study performed similarly to Murugan et al. [18] with Euler simulation had shown that the shock/blast wave evolution is exactly similar when the grid was doubled.

Results and Discussion

Figures 3, 4 and 5 show the evolution of blast wave with density gradient magnitude contours along with line plots at different lateral planes for three objects to visualize the blast wave interaction with the objects. Here the blast wave Mach number (M) is calculated just ahead of the objects. The legends in density gradient plots are kept same to compare the strength of blast wave during interaction. Here D is the diameter of the shock tube (100 mm), and L is the axial distance from the leading edge of the objects and Y is the radial distance. The line plots are made by extracting

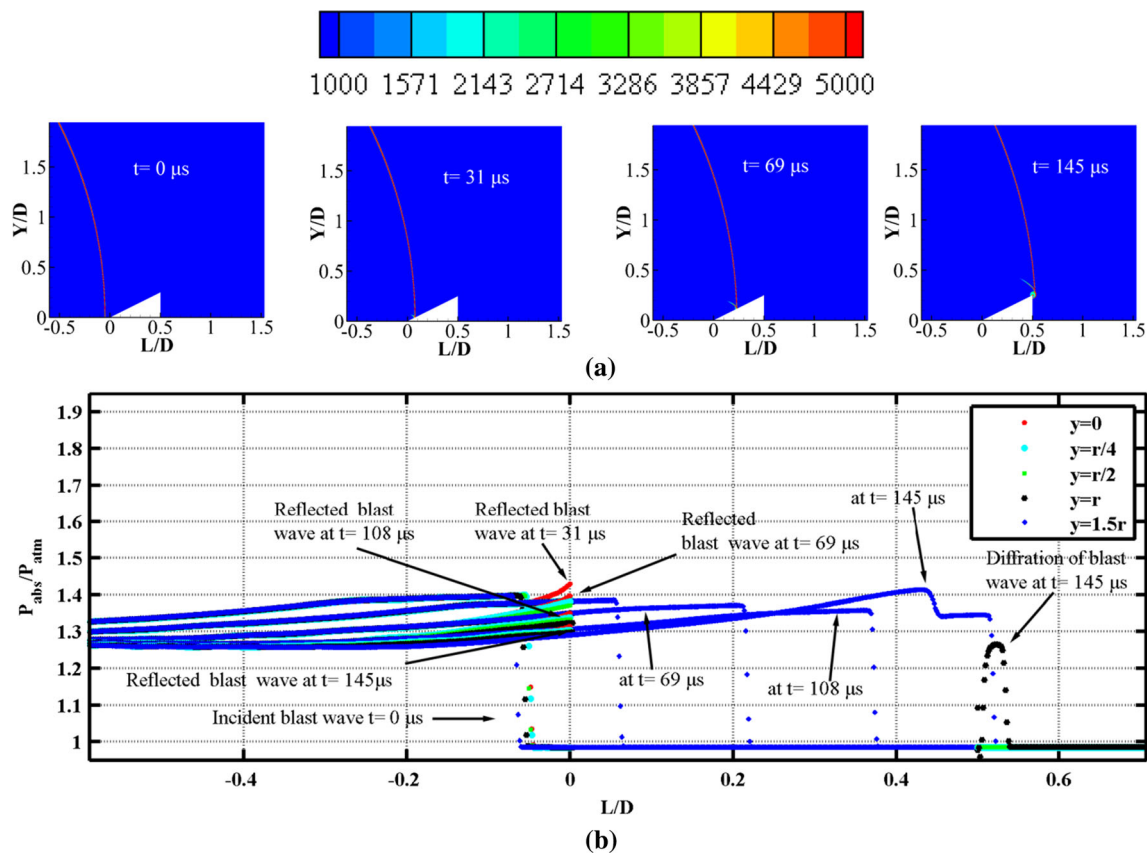


Fig. 4 **a** Density gradient magnitude plots and **b** pressure plot showing blast wave interaction with cone for t varying from 0 to 145 μs

the static pressures at four planes ($y = 0$, $r/4$, $r/2$, r , and $1.5r$) along the downstream direction where r is the height/radius of the objects.

Blast Wave Interaction with Objects

Figure 3 shows the interaction of blast wave with the cylindrical object. The time at which the blast wave is at $L/D = -0.07$ is taken as zero ($t = 0$). A portion of the blast wave gets reflected after the blast wave impinges on the front portion of the cylindrical object which is shown at $t = 26 \mu\text{s}$. This causes a sudden increase in the pressure ahead of the cylinder as the flow comes to rest. The upstream movement of the reflected blast wave from the cylinder with time is seen along the $y = 0$ plane. The strength of the reflected blast wave from the cylinder reduces due to the expansion of the blast wave with an increase in the upstream direction. A much-reduced strength of this reflected shock at $y = r$ is mainly due to the spherical expansion of the reflected shock near the front edge of the cylinder. The reduction in strength at $y = 1.5r$ is huge compared to the axial region, and the blast

wave moves ahead as a weak blast wave as shown in Fig. 3b.

The diffraction blast wave at the front sharp corner causes a flow separation which subsequently develops into a corner vortex. This blast wave further gets diffracted at the rear end of the cylinder due to sudden expansion resulting from the backward step ($t = 177 \mu\text{s}$). A great reduction in blast strength behind the cylinder due to diffraction can be seen after $L/D = 0.5$ in Fig. 3b. However, the strength of the blast wave at $y = 1.5r$ is unaffected by the expansion at $y = r$. Figure 4 shows the interaction of blast wave with the conical object for $M = 1.15$. Unlike the cylindrical object where the reflected shock strength is increased to 1.9, the reflected blast wave is very weak here ($P_{\text{abs}}/P_{\text{atm}} = 1.42$) due to the sharp edge and a small deflection angle. It becomes an acoustic wave and moves along the upstream direction, and it is not seen in Fig. 4a due to negligible rise in pressure. The strength of the blast wave passes over the cone is increased as it reaches the rear end of the cone due to a continuous rise in blast wave strength over the cone resulting from the reduction in area. This can be seen from pressure plot at $y = 1.5r$ in Fig. 4b. The blast wave gets diffracted behind the cone similar to

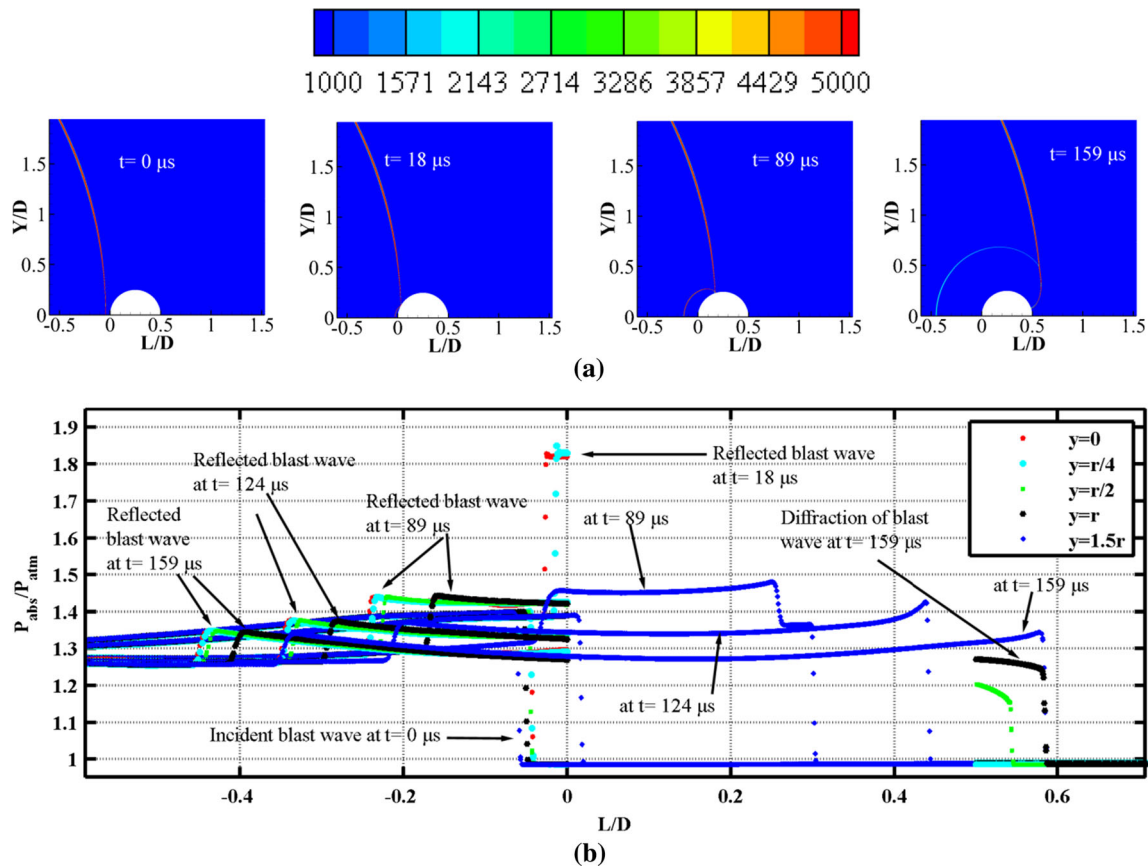


Fig. 5 a Density gradient magnitude plots and b blast wave interaction with sphere for t varying from 0 to 159 μs

cylinder upon reaching the sharp corner at $L/D = 0.5$. This results in the formation of a vortex from the slip line at $t = 145 \mu s$ which has been observed in many earlier studies [26–28].

Figure 5 shows the interaction of the blast wave with sphere for $M = 1.15$. Here, the strength of the reflected blast wave (P_{abs}/P_{atm}) reaches up to 1.82 which is close to 1.91 obtained in case of the cylindrical object. The strength of the reflected shock obtained at different upstream locations for $t = 18 \mu s$, $89 \mu s$, $124 \mu s$, and $159 \mu s$ is also less compared to the cylinder. Though a gradual rise in strength of the incident blast wave is seen at $y = 1.5r$ up to the maximum height of the sphere, the diffraction of the blast wave at the maximum radius is not significant compared to the other objects. This is due to a gradual change in the area from the top portion of the sphere. Hence the slipstream vortex is absent which shows a least energy loss for the blast wave compared to the other objects. The blast wave moves towards the axis as an expansion wave over the sphere surface which is seen in Fig. 5a.

Blast Wave Reattachment Behind the Objects

The location of blast wave reattachment behind the objects provides information about the amount of pressure energy lost due to reflection, diffraction, and production of vorticity. The blast wave reattachment distance depends on the amount of pressure energy lost during interaction as it affects the velocity of the blast wave behind the objects. It is discussed in the subsequent section for three objects.

Blast Wave Reattachment for Cylinder

Figures 6, 7 and 8 show the blast wave pressure histories for cylinder from $t = 220 \mu s$ to $638 \mu s$. The blast wave moving towards the axis at $t = 177 \mu s$ in Fig. 3 gets reflected from the symmetrical plane at $t = 220 \mu s$ in Fig. 6. It is observed between the non-dimensional distance (L/D) 0.5 to 0.6. A change in blast wave curve behind the cylinder in the inward direction shows this reduction in blast wave speed due to expansion. It is seen at $t = 220 \mu s$ ($y = 0$) where the blast wave is far behind in comparison to the other sectional planes. The reflected blast wave from the axis expands spherically, and a part of it superimposes

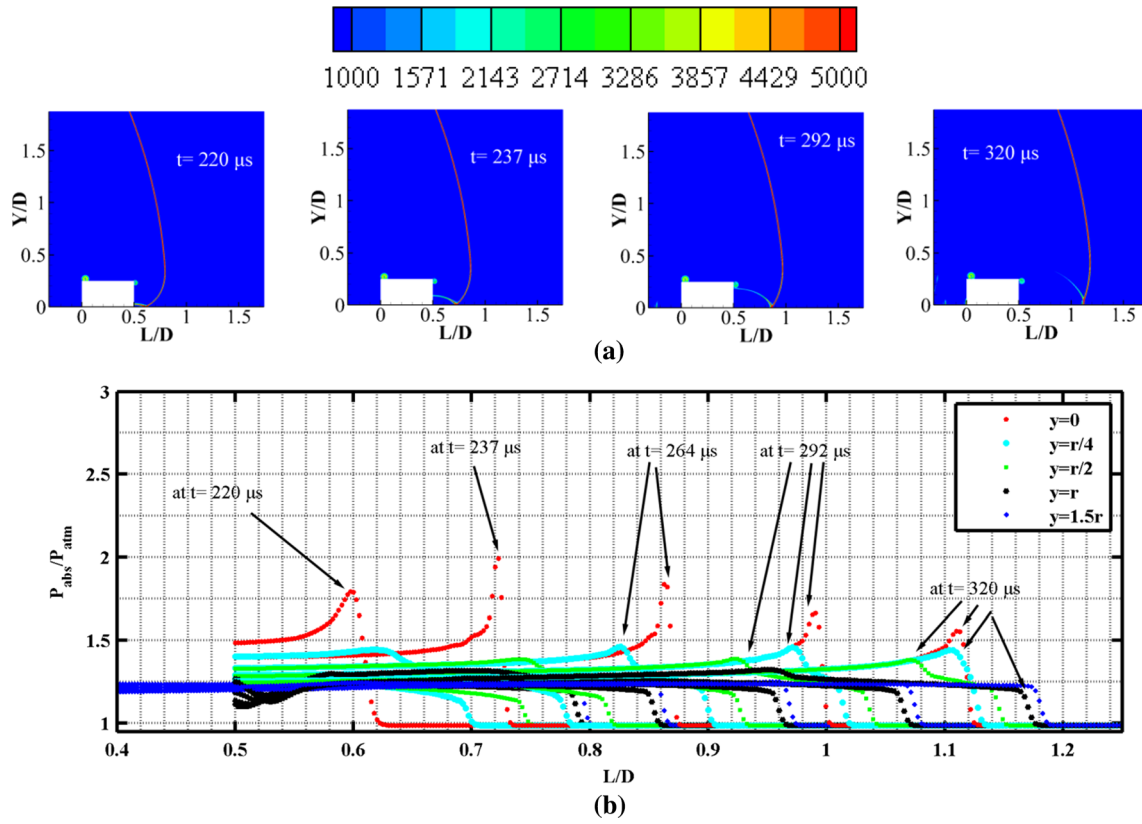


Fig. 6 a Density gradient magnitude and b blast wave pressure history plots for time varying from 220 to 320 μs for cylinder

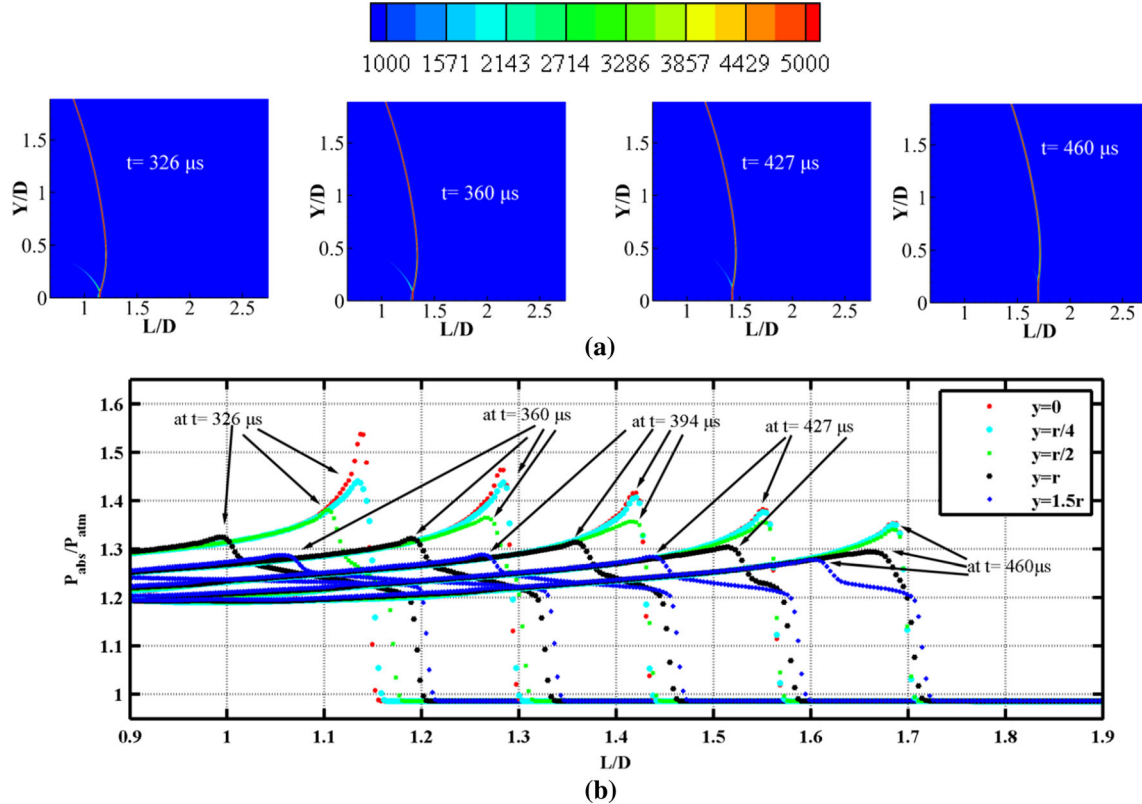


Fig. 7 a Density gradient magnitude and b blast wave pressure history plots for time varying from 326 to 460 μs for cylinder

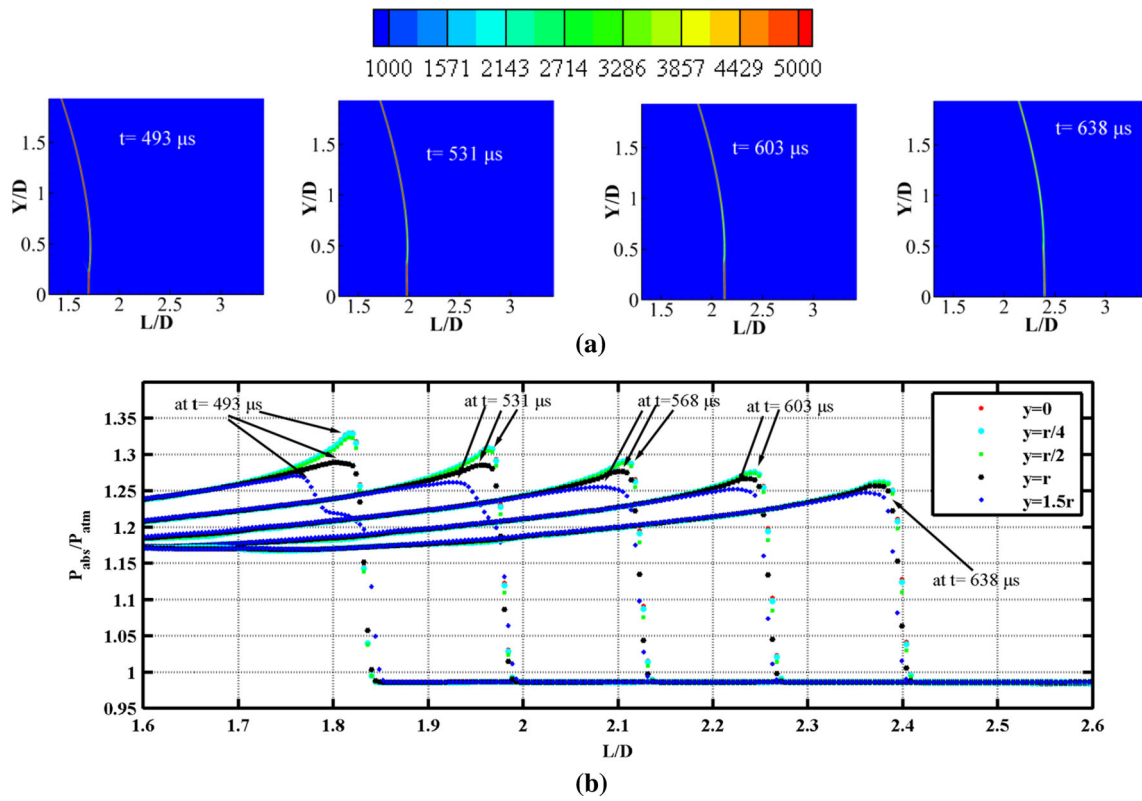


Fig. 8 a Density gradient magnitude and b blast wave pressure history plots for time varying from 493 to 638 μs for cylinder

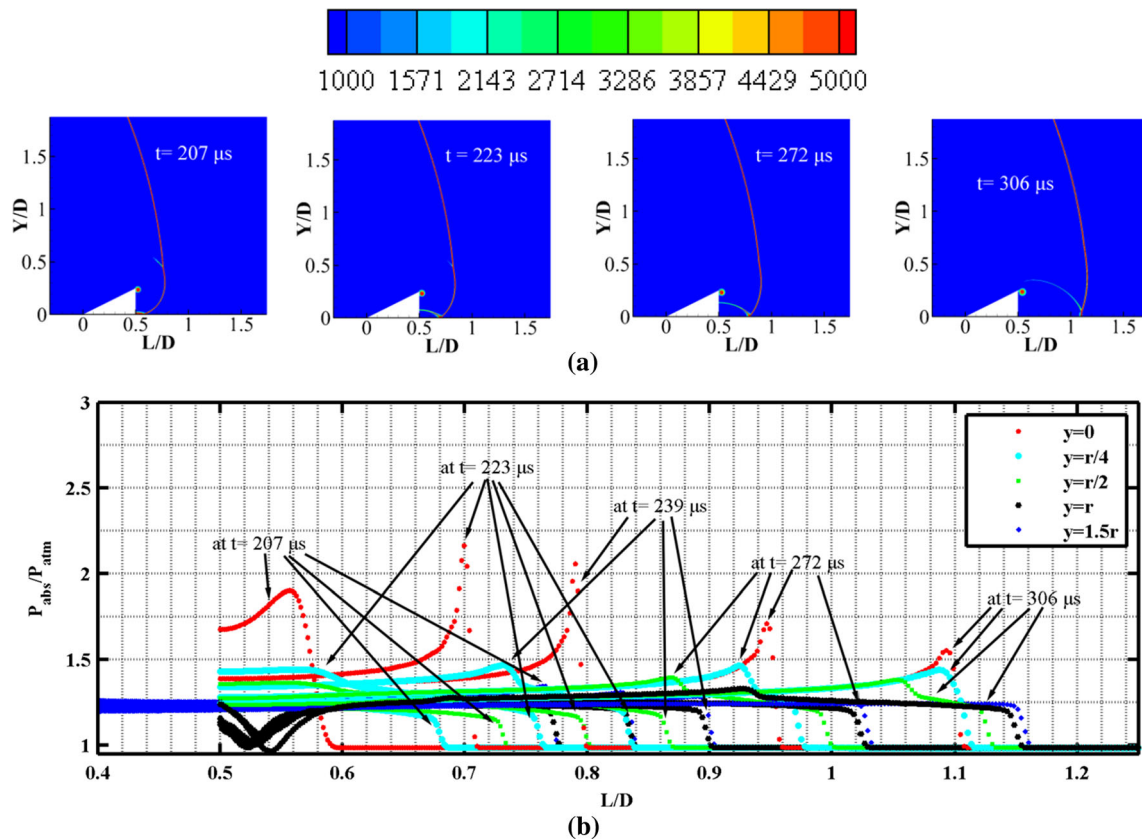


Fig. 9 a Density gradient magnitude and b blast wave pressure history plots for time varying from 207 to 306 μs for cone

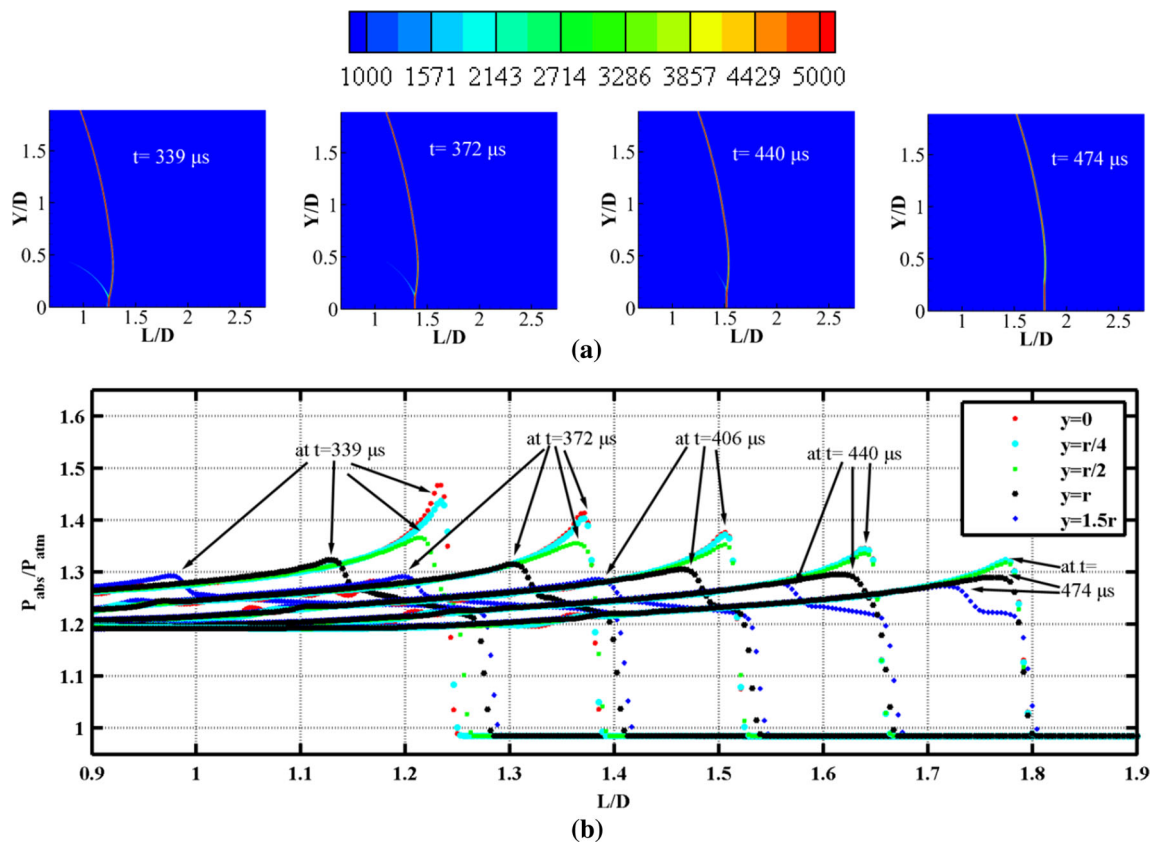


Fig. 10 **a** Density gradient magnitude and **b** blast wave pressure history plots for time varying from 339 to 474 μs for cone

with the down running incident blast wave ($t = 237 \mu\text{s}$). The weak link of the incident blast wave behind the axis gains strength and momentum due to superimposition of this reflected blast wave ($t = 292 \mu\text{s}$). Hence, the blast wave in the axial region moves faster compared to the other sections, and this phenomenon helps in regenerating the blast wave. It is seen at $t = 264$ and $292 \mu\text{s}$ where the diffracted blast wave catches up with the blast wave at other sections.

Figure 7 shows the superimposition of reflected blast wave at other parts of the incident blast wave at later times from $t = 326$ to $460 \mu\text{s}$. The superimposition of reflected blast wave produces a much uniform blast wave profile in the axial region, and it can be seen in both density gradient and pressure plots. A continuous reduction in spacing between the blast wave profile at different planes in Fig. 7b shows the reattachment of blast wave in the axial region. The superimposition of blast waves from four lateral planes is clearly seen in Fig. 8 where the blast wave at $t = 638 \mu\text{s}$ is almost reattached with incident wave.

Blast Wave Reattachment for Cone

Figures 9, 10 and 11 show the propagation of incident and reflected blast wave behind the cone from $t = 207$ to $306 \mu\text{s}$ at $M = 1.15$. The blast wave gets reflected from the symmetrical plane at $t = 207 \mu\text{s}$ similar to the cylindrical object. The strength of reflected blast wave at $t = 207 \mu\text{s}$ and $223 \mu\text{s}$ in Fig. 9b is large compared to the cylinder in Fig. 6b. This causes a faster superimposition of reflected blast wave with the incident wave at $y = r/4$ ($t = 306 \mu\text{s}$) in Fig. 9b compared to the cylinder. The vortex formed at the slipstream is continued to grow from $t = 207$ to $306 \mu\text{s}$ which takes a longer time to detach from the cone.

Figures 10 and 11 show the regeneration of blast wave in the axial region of the cone from time $t = 339$ to $648 \mu\text{s}$. A clear superimposition of waves in the axial region is seen at $L/D = 1.93$ ($t = 508 \mu\text{s}$) in Fig. 11b. However, a similar profile is seen at $L/D = 2.13$ ($t = 568 \mu\text{s}$) in Fig. 8b for cylinder. It suggests that the regeneration blast wave takes place much earlier with conical object compared to the cylinder. It can be attributed to the larger pressure loss in the cylinder due to the stronger reflected blast wave and production of vorticity at two sharp corners.

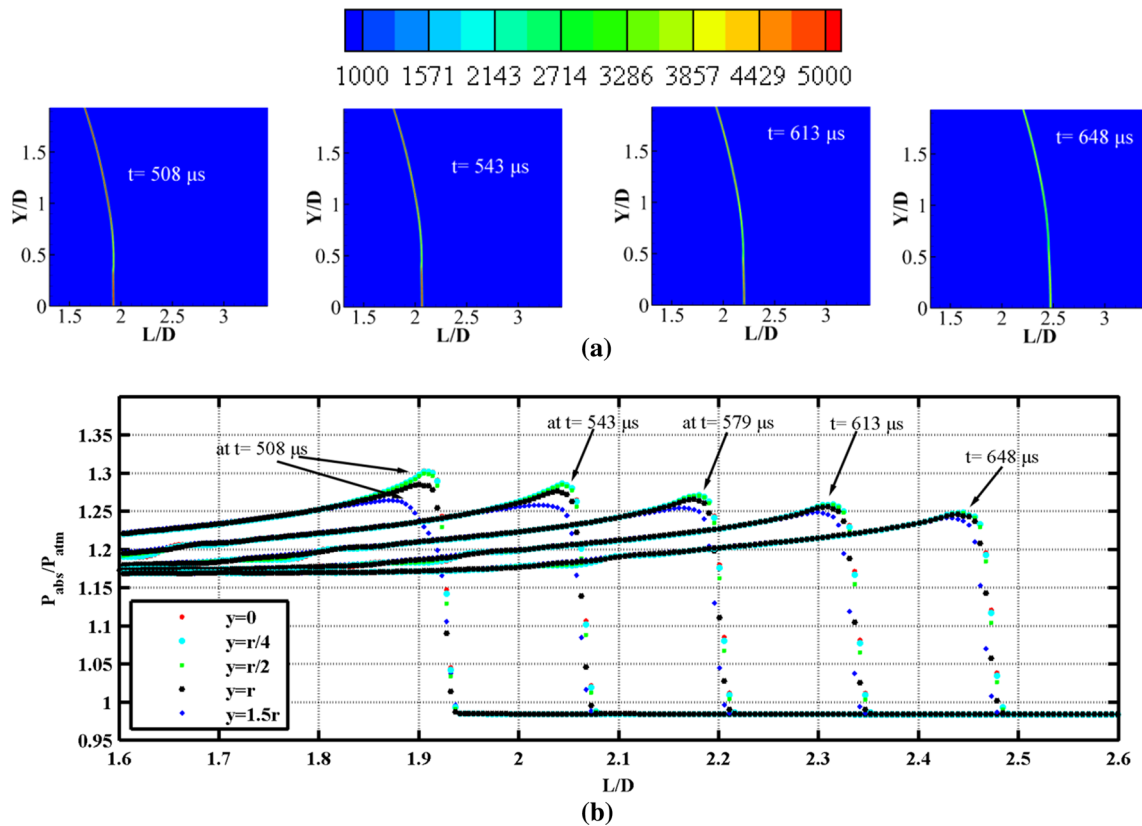


Fig. 11 a Density gradient magnitude and b blast wave pressure history plots for time varying from 493 to 648 μ s for the cone

Blast Wave Reattachment for Sphere

Figure 12 shows the evolution of the reflected and incident blast waves behind the sphere for time varying from 189 to 311 μ s. It is interesting to see that the strength of the reflected blast wave (P_{abs}/P_{atm}) along $y = 0$ (symmetrical plane) close to $L/D = 0.6$ is 2.7. However, it is 1.85 and 1.6 for conical and cylindrical objects. It suggests that a least amount of blast energy is lost when the blast wave passes over the spherical object. Hence, the regeneration of blast wave takes much faster for sphere compared to other objects due to the superimposition of the stronger reflected blast wave.

Figures 13 and 14 show the superimposition of blast wave in the axial region from $t = 342$ to 649μ s. It is clearly seen in Fig. 13b that the uniform pressure profile in the axial region is noticed at $L/D = 1.83$ ($t = 478 \mu$ s) which is a less distance compared to the cone ($L/D = 1.93$) and cylinder ($L/D = 2.13$). The formation of uniform pressure profile at these four lateral planes for different objects along the axis does not ensure the generation of spherical pressure profile which would take little longer distance. However, the sensors placed at least after these locations could provide the blast wave strength with the

uncertainty of less than 5% which is acceptable in experiments.

Conclusions

The blast wave generated from a short driver section shock tube and its interaction with three objects has been studied for an incident blast wave Mach number of 1.15 through numerical simulation using commercial software ANSYS Fluent. The computational analysis reveals that the initial reflection is the strongest in case of cylinder followed by the sphere, and it is least in the cone. Slipstream vortices are noticed at sharp corners in both cylinder and cone after diffraction, and it is not observed over sphere due to gradual change in surface area. In all the cases, a reflection of blast wave is noticed at the symmetrical plane, and it expands spherically. A portion of the reflected blast wave moving along the downstream direction superimposes with the incident blast wave and enhances its strength in the wake region of the objects. This causes an increase in the strength of the wave moving behind the objects which subsequently regenerates the spherical blast wave observed before the interaction. The pressure histories obtained at

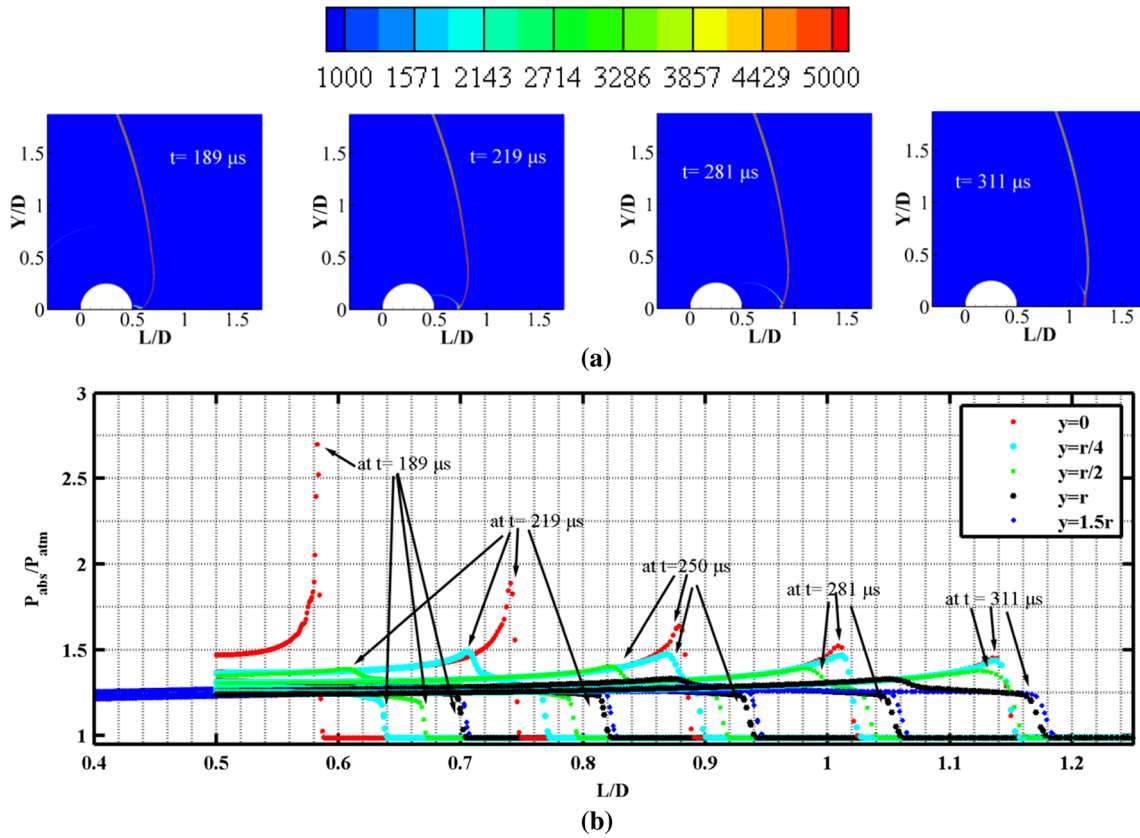


Fig. 12 a Density gradient magnitude and b blast wave pressure history plots for time varying from 189 to 311 μs for sphere

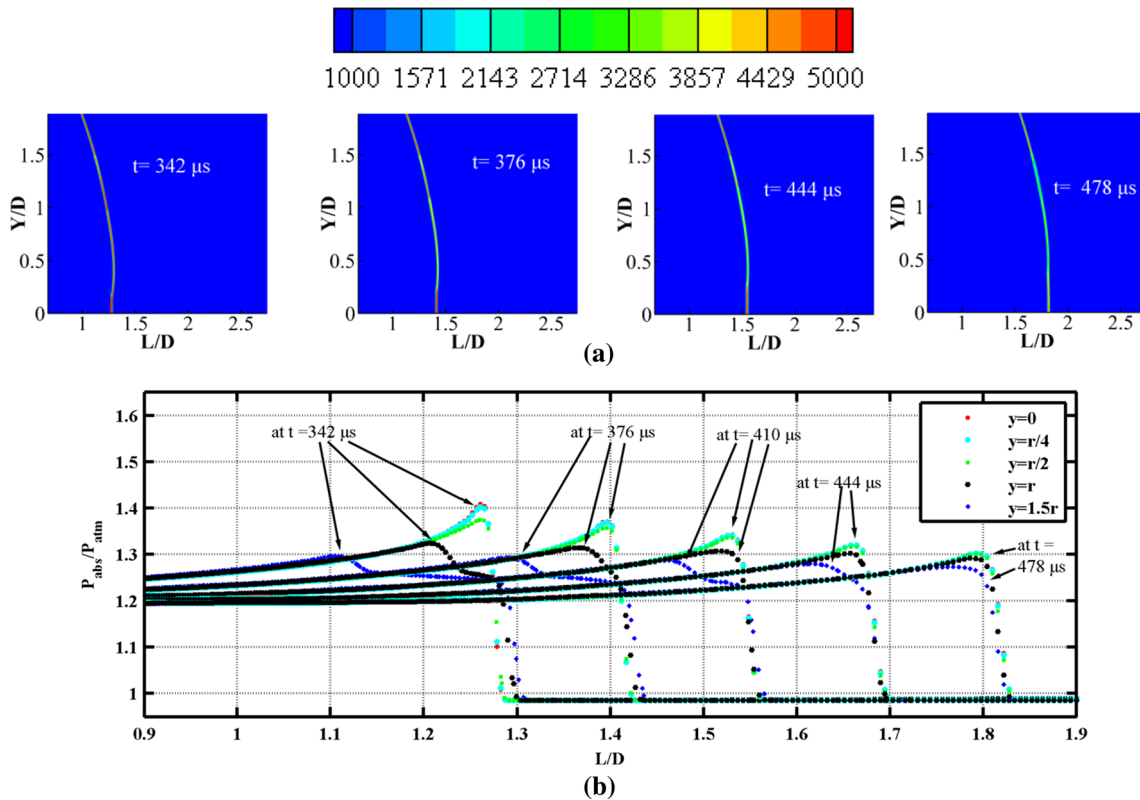


Fig. 13 a Density gradient magnitude and b blast wave pressure history plots for time varying from 342 to 478 μs for sphere

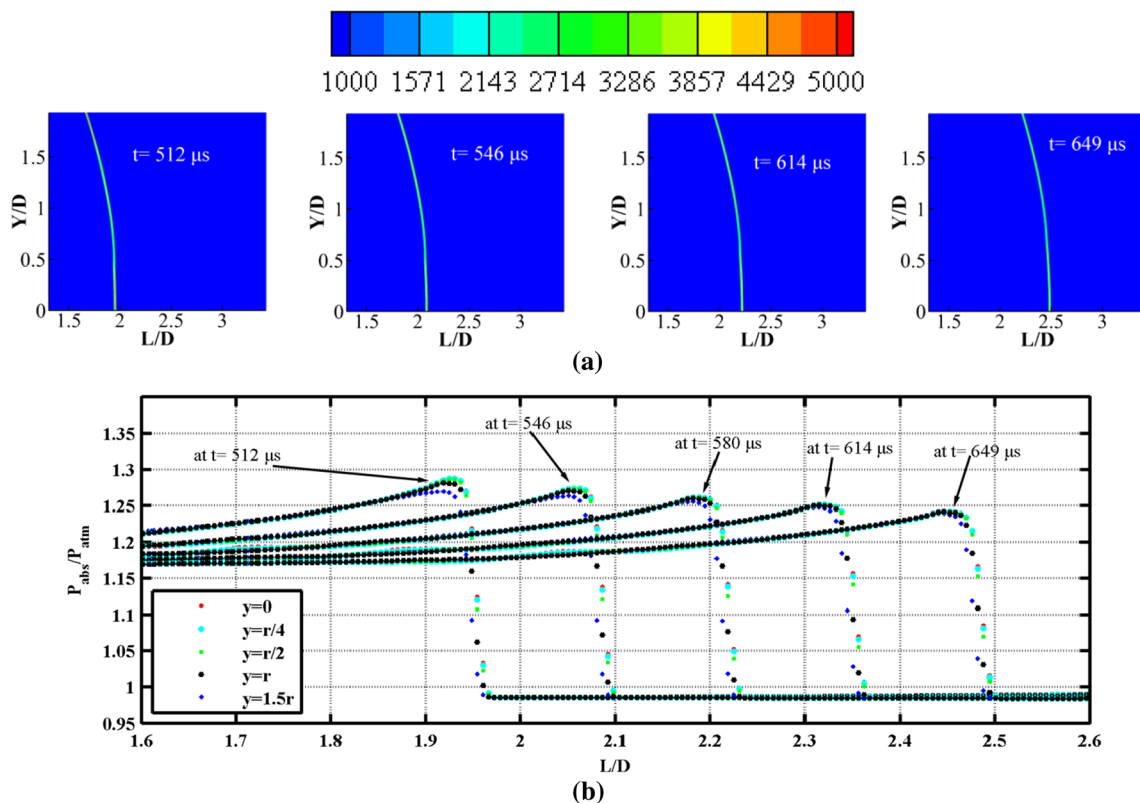


Fig. 14 **a** Density gradient magnitude and **b** blast wave pressure history plots for time varying from 512 to 649 μs for sphere

four lateral planes for three objects reveal that the regeneration of uniform blast wave took place much earlier in sphere compared to the cylinder and cone. It is expected that the regeneration takes longer distance for cylinder due to the formation of strong reflected shock and diffraction at two sharp corners. Similarly, it is expected that sphere may take longer distance due to the formation of strong reflected shock. However, the diffraction and vorticity production at the sharp corner dominate the pressure loss of the blast wave and delay the regeneration. The non-dimensional distances of uniform blast wave pressure profile generation are 2.13, 1.93 and 1.83 for the cylinder, cone, and sphere, respectively. Hence, the sensors placed after these locations for the above objects could provide the blast wave peak overpressure and impulse with less than 5% uncertainties.

Acknowledgements Authors sincerely acknowledge the TBRL, Chandigarh, India, for their partial financial support for this work. Authors thank Dr. Anupam Sinha for his support in simulation at high-performance computational facility of CSIR-CMERI. We also acknowledge Mr. Ajay Kuchlyan for his support in post-processing.

References

1. A.M. Remennikov, Modelling blast loads on buildings in complex city geometries. *Comput. Struct.* **83**, 2197–2220 (2005). <https://doi.org/10.1016/j.compstruc.2005.04.003>
2. I.G. Cullis, Blast waves and how they interact with structures. *J. R. Army Med. Corps* **147**, 16–26 (2001). <https://doi.org/10.1136/jramc-147-01-02>
3. N. Michael, *Visual Model for Blast Waves and Fracture* (Department of Computer Science, University of Toronto, Toronto, 1998)
4. G. Chen, M. Feldman, Free boundary problems in shock reflection/diffraction and related transonic flow problems. *Philos. Trans. R. Soc. A* **373**, 20140276 (2015). <https://doi.org/10.1098/rsta.2014.0276>
5. A.E. Bryson, R.W.F. Gross, Diffraction of strong shocks by cones, cylinders, and spheres. *J. Fluid Mech.* **10**, 1–16 (1961). <https://doi.org/10.1017/S0022112061000019>
6. G.B. Whitham, A new approach to problems of shock dynamics part I two-dimensional problems. *J. Fluid Mech.* **2**, 145–171 (1957). <https://doi.org/10.1017/S002211205700004X>
7. G.B. Whitham, A new approach to problems of shock dynamics part II two-dimensional problems. *J. Fluid Mech.* **5**, 369–386 (1959). <https://doi.org/10.1017/S002211205900026X>
8. M. Sun, T. Saito, K. Takayama, H. Tanno, Unsteady drag on a sphere by shock wave loading. *Shock Waves* **14**, 3–9 (2005). <https://doi.org/10.1007/s00193-004-0235-4>
9. K. Kontis, R. An, J.A. Edwards, Compressible vortex ring studies with a number of generic body configurations. *AIAA J* **44**, 2962–2978 (2006). <https://doi.org/10.2514/1.21018>
10. T. Murugan, D. Das, Experimental study on a compressible vortex ring in collision with a wall. *J. Vis.* **15**(4), 321–332 (2012). <https://doi.org/10.1007/s12650-012-0138-x>
11. T. Murugan, S. De, A. Sreevatsa, S. Dutta, Numerical simulation of compressible vortex–wall interaction. *Shockwaves* **26**(3), 311–326 (2016). <https://doi.org/10.1007/s00193-015-0611-2>
12. T. Murugan, S. De, A. Kundu, I.P.S. Sandhu, D.R. Saroha, Interaction of a shock tube generated blast wave with solid

- obstacles, in *11th International High Energy Materials Conference & Exhibits, 23–25 November, Pune, India* (2017)
13. S. Dey, T. Murugan, D. Chatterjee, Numerical visualization of blast wave interacting with objects. *J. Appl. Fluid. Mech.* **11**(5), 1201–1206 (2018)
 14. N. Chandra, S. Ganpule, N.N. Kleinschmit, R. Feng, A.D. Holmberg, A. Sundaramurthy, V. Selvan, A. Alai, Evolution of blast wave profiles in simulated air blasts: experiment and computational modeling. *Shock Waves* **22**, 403–415 (2012). <https://doi.org/10.1007/s00193-012-0399-2>
 15. T. Murugan, S. De, C.L. Dora, D. Das, Numerical simulation and PIV study of compressible vortex ring evolution. *Shock Waves* **22**, 69–83 (2012). <https://doi.org/10.1007/s00193-011-0344-9>
 16. T. Murugan, Flow and acoustic characteristics of high Mach number vortex rings during evolution and wall-interaction: an experimental investigation. Ph.D. thesis, Indian Institute of Technology, Kanpur (2008)
 17. S. De, T. Murugan, Numerical simulation of shock tube generated vortex: effect of numerics. *Int. J Comput Fluid Dyn.* **25**, 345–354 (2011). <https://doi.org/10.1080/10618562.2011.600694>
 18. T. Murugan, S. De, C.L. Dora, D. Das, P.P. Kumar, A study of the counter rotating vortex rings interacting with the primary vortex ring in shock tube generated flows. *Fluid Dyn. Res.* **45**(2), 025506 (2013). <https://doi.org/10.1088/0169-5983/45/2/025506>
 19. Ansys Fluent, ver. 13, *Theory Guide* (Ansys Inc., Washington, 2011)
 20. R. Ishii, H. Fujimoto, N. Hatta, Y. Umeda, Experimental and numerical analysis of circular pulse jets. *J. Fluid Mech.* **392**, 129–153 (1999). <https://doi.org/10.1017/S0022112099005303>
 21. K. Takayama, T. Saito, M. Sun, K. Tamai, H. Tanno, J. Falcovitz, Unsteady drag force measurements of shock loaded bodies suspended in a vertical shock tube, in *Proceedings of the 21st International Congress of Theoretical and Applied Mechanics, Warsaw, Poland* (2004)
 22. M.-S. Liou, C. Steffen, A new flux splitting scheme. *J. Comput. Phys.* **107**, 23–39 (1993). <https://doi.org/10.1006/jcph.1993.1122>
 23. V. Kumar, M. Singh, T. Murugan, P.K. Chatterjee, Effect of free stream turbulence on flow past a circular cylinder at low Reynolds numbers. *J. Inst. Eng. India Ser. C.* (2018). <https://doi.org/10.1007/s40032-017-0422-6>
 24. A. Kundu, S. De, T. Murugan, C.L. Dora, D. Das, Numerical visualization of shock tube-generated vortex–wall interaction using a fifth-order upwind scheme. *J. Vis.* **19**(4), 667–678 (2016). <https://doi.org/10.1007/s12650-016-0362-x>
 25. C.L. Dora, T. Murugan, S. De, D. Das, Role of slipstream instability in formation of counter-rotating vortex rings ahead of a compressible vortex ring. *J. Fluid Mech.* **753**, 29–48 (2014). <https://doi.org/10.1017/jfm.2014.353>
 26. G. Abate, W. Shyy, Dynamic structure of confined shocks undergoing sudden expansion. *Prog. Aerosp. Sci.* **38**, 23–42 (2002). [https://doi.org/10.1016/S0376-0421\(01\)00016-1](https://doi.org/10.1016/S0376-0421(01)00016-1)
 27. M. Sun, K. Takayama, A note on numerical simulation of vortical structures in shock diffraction. *Shock Waves* **13**, 25–32 (2003). <https://doi.org/10.1007/s00193-003-0195-0>
 28. T.-I. Tseng, R.-J. Yang, Numerical simulation of vorticity production in shock diffraction. *AIAA J.* **44**(5), 1040–1047 (2006). <https://doi.org/10.2514/1.16196>

Publisher's Note Springer Nature remains neutral with regard to jurisdictional claims in published maps and institutional affiliations.